Dual-Mode Deep Anomaly Detection for Medical Manufacturing: Structural Similarity and Feature Distance

Julio Zanon Diaz[1], Georgios Siogkas[2], and Peter Corcoran[1], Fellow IEEE.
[1]Electrical and Electronic Engineering, University of Galway, Galway, Ireland.
[2]Boston Scientific, Galway, Ireland.

Corresponding author: Julio Zanon Diaz (j.zanondiaz1@UniversityofGalway.ie).

This work was supported in part by the Galway Boston Scientific's manufacturing facility.

ABSTRACT Automating visual inspection in medical device manufacturing remains challenging due to small and imbalanced datasets, high-resolution imagery, and stringent regulatory requirements. This work proposes two attention-guided autoencoder architectures for deep anomaly detection designed to address these constraints. The first employs a structural similarity–based anomaly score (4-MS-SSIM), offering lightweight and accurate real-time defect detection, yielding ACC 0.903 (unsupervised thresholding) and 0.931 (supervised thresholding) on the "Surface Seal Image" Test split with only 10% of defective samples. The second applies a feature-distance approach using Mahalanobis scoring on reduced latent features, providing high sensitivity to distributional shifts for supervisory monitoring, achieving ACC 0.722 with supervised thresholding. Together, these methods deliver complementary capabilities: the first supports reliable inline inspection, while the second enables scalable post-production surveillance and regulatory compliance monitoring. Experimental results demonstrate that both approaches surpass re-implemented baselines and provide a practical pathway for deploying deep anomaly detection in regulated manufacturing environments, aligning accuracy, efficiency, and the regulatory obligations defined for high-risk AI systems under the EU AI Act.

INDEX TERMS Machine Vision, Deep Anomaly Detection, Neural Networks, Advanced Manufacturing, Quality Control.

I. INTRODUCTION

The advent of digital manufacturing, characterised by the integration of automation technologies, seeks to significantly transform traditional manufacturing processes. This transition, driven by Industry 4.0, is anticipated to enhance productivity, efficiency, and responsiveness to market demands. Key elements for achieving this transformation include the development and successful implementation of advanced visual-cognitive systems based on machine vision and Convolutional Neural Networks (CNNs). These systems are tasked with learning complex visual features from images and making rational decisions that align with human cognitive abilities.

A notable application of these technologies is the automation of visual inspections in manufacturing processes, aimed at identifying defects in products. This is particularly critical in highly regulated industries such as Medical Devices, where the severity of False Negatives (FN) could have serious implications for patient health and wellbeing. Furthermore, highly regulated industries encounter challenges including a minimal incidence of naturally occurring defects and the distinctiveness of each process, which influence overall production volumes and the capability to compile comprehensive datasets within feasible timeframes.

In the context of this work, the task under investigation is binary classification—determining whether a part is acceptable (defect-free) or defective. While other research has focused on defect segmentation, which provides spatial localisation of anomalies, we emphasise that in regulated manufacturing the primary risk lies in ensuring that all defective parts are reliably detected and removed from production. From a quality and regulatory perspective, false negatives (missed defects) present the most critical failure mode. Segmentation can provide

additional value for root-cause analysis and process improvement, but such benefits must not come at the expense of classification accuracy. For this reason, our research prioritises robust defect classification, aligning with the fundamental requirement that defective parts be identified and scrapped.

While visual-cognitive technologies in manufacturing, particularly Convolutional Neural Networks (CNNs), are an active field of research, numerous limitations and unresolved challenges remain. These factors currently render these technologies suboptimal for wide adoption in manufacturing environments. In the absence of adequate solutions to automate visual inspections, the manufacturing industry, particularly the Medical Device industry and other highly regulated sectors, relies on Human Visual Inspections (HVIs). Rodriguez-Perez [1] underscores this reliance and discusses the significant prevalence of human errors in medical device manufacturing and pharmaceutical companies, estimating that these errors account for one-third of all non-conformances.

In previous research related to this article, we investigated the application of state-of-the-art Convolutional Neural Networks (CNNs) to identify defects in the seals of sterile packaging [2]. We considered this use-case representative of Medical Device manufacturing inspection due to the subjective nature of defect definition and the criticality of False Negatives (FNs). To conduct this research, we developed a methodology to create the "Surface Seal Image (SSI)" dataset [3] that accurately represents real-world manufacturing defects. Key findings from our research include:

Due to the typical low defect rate in manufacturing, datasets are not only small but also unbalanced, with a very limited number of defect samples.

Typical manufacturing images used for inspections, such as those in the SSI dataset, exhibit low pixel complexity and content variation, which renders basic augmentation techniques or deep CNN architectures suboptimal for this task.

State-of-the-art models demonstrated success in classifying defects when trained with small and moderately skewed datasets, but their performance declined when defect samples only constituted around 10% of all images in small datasets.

This article focuses on researching Convolutional Neural Networks (CNNs) to enhance defect detection performance when trained on small datasets with a 10% defect imbalance. Specifically, we will examine methodologies that rely on defect-free images to take advantage of the 90% of images with no defects as well as generic approaches that necessitate minimal domain-specific optimisation and can be scaled across industries such as Medical Devices, where processes are highly specialised.

The Surface Seal Image (SSI) dataset [3], particularly the "Partial-10" subset containing only 10% of defects, will serve as a baseline for performance assessment.

II. BACKGROUND AND LITERATURE REVIEW

Traditional Convolutional Neural Networks (CNNs) achieve state-of-the-art performance when trained on large, balanced datasets containing many examples of each class. However, as shown in our previous work [2] and other studies such as Yuan and Zuo [8], CNN classification accuracy drops significantly when trained on small datasets. This limitation is particularly acute in regulated manufacturing environments, where naturally occurring defects are rare and labelled defect images are scarce.

In this section, we first review existing methodologies developed to address small dataset challenges (Section A). We then introduce anomaly detection and explain why this approach is relevant to our work (Section B). Section C discusses deep anomaly detection, focusing on representative architectures from the literature. Section D summarises key insights.

A. SMALL DATASETS - METHODOLOGIES TO OPTIMISE PERFORMANCE OF DEEP LEARNING MODELS

There are three well-established methods for improving deep neural network performance when training data are limited: transfer learning, meta-learning, and data augmentation.

Transfer Learning:

Transfer Learning, introduced by Bozinovski and Fulgosi [9], enables models to reuse pretrained weights from one domain to accelerate training and improve performance on another. It is widely applied in vision tasks [10], reducing computational costs and training time [11]. In medical imaging, Transfer Learning has shown benefits in tasks such as MRI-based tumour detection [12]–[14]. However, accuracy remains well below the near-perfect levels required in highly regulated manufacturing. Moreover, domain similarity is critical: while medical imaging tasks share strong structural resemblance, defect inspection in manufacturing is far less correlated with ImageNet-style pretraining as industrial imagery lacks semantic richness and instead emphasises local texture irregularities. Coupled with the absence of large defect datasets in manufacturing, Transfer Learning was judged insufficient for this study.

Meta-Learning Based Architectures

Meta-learning, or "learning to learn," aims to generalise from very few labelled samples. Approaches such as Siamese

networks [15] and Triplet-Graph Reasoning Networks (TGRN) [16] have demonstrated success in few-shot defect inspection, segmenting anomalies with as few as 1–4 labelled samples. However, our work targets datasets with several hundred defect-free samples. Under these conditions, meta-learning is less effective than approaches that exploit the abundant normal images.

Dataset Augmentation

Data augmentation artificially increases dataset size by generating new image variants. Introduced by Krizhevsky et al. [17] and widely applied in medical imaging [18], augmentation can improve model robustness. Yet, in manufacturing images such as those in the SSI dataset [3], low pixel complexity and limited variation mean basic augmentations degrade rather than enhance performance [2], as they introduce artificial variability not present in tightly controlled industrial imaging environments. Generative augmentation methods such as Defect-GAN [19] offer potential, but these also require large training datasets, which are not available in our case.

B. ANOMALY DETECTION

Anomaly detection, also referred to as novelty or outlier detection, identifies samples that deviate from normality. Applications span multiple domains, including fraud detection, medical diagnosis, and industrial fault analysis. In image-based inspection, anomaly detection typically involves:

1. Training a feature extractor on normal (defect-free) images.
2. Comparing features of new samples to the learned distribution of normality.

This approach is appealing for regulated manufacturing, as it exploits abundant defect-free data, avoids the need for extensive labelling, and reduces the risk of overfitting. Figure 1 illustrates a generic unsupervised anomaly detection pipeline.

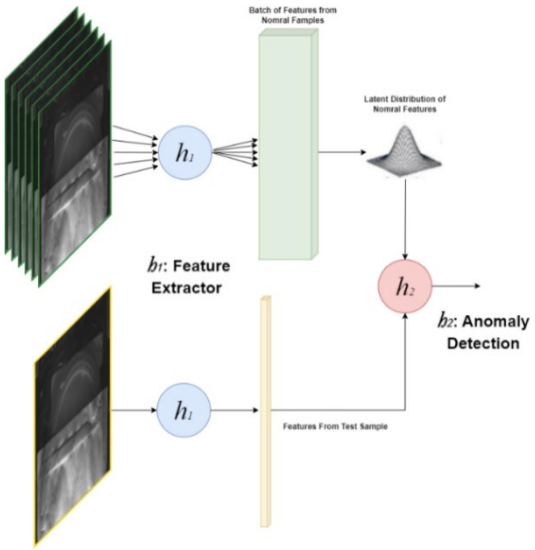

Figure 1 ***Spatial Data - Unsupervised Anomaly Detection***

Historically, feature extraction relied on detectors such as GFTT [20], MSER [21], and FAST [22], combined with descriptors like BRIEF [23] or FREAK [24]. Later methods such as SIFT [25] and SURF [26] integrated detection and description, becoming standard baselines. With advances in computing, CNN-based descriptors surpassed hand-crafted features, e.g., DeepPatch [27], LIFT [28], and R2D2 [29], all demonstrating superior invariance and discriminative power.

Among modern feature extractors, Convolutional Autoencoders (CAEs) have gained popularity due to their ability to learn compact, non-linear representations in an end-to-end manner [30]–[32]. CAEs are effective for dimensionality reduction and denoising, making them suitable for modelling normal data distributions. Variational Autoencoders (VAEs) [33] extend CAEs by introducing probabilistic latent variables but require more complex tuning and often yield marginal improvements.

C. DEEP ANOMALY DETECTION

Deep Anomaly Detection incorporates CNNs or CAEs into anomaly detection pipelines. A simple form is the Vanilla Autoencoder, which reconstructs normal samples and identifies anomalies via high reconstruction loss [34]. Hybrid approaches extend this by applying anomaly scoring functions directly to latent features [35].

Several more advanced architectures have been proposed:

MOCCA (Multilayer One-Class Classification): Introduced by Massoli et al. [36], MOCCA employs a deep autoencoder with additional centroid-based loss functions to compress latent feature distributions. While effective, this requires extensive computational resources, limiting industrial deployment.

CPCAE (Conditional Patch-based CAE): Saeedi and Giusti [37] adapt CAEs for high-resolution inspection by dividing images into overlapping patches with positional encoding. Reconstruction errors are then classified using features from pretrained networks. This approach preserves spatial detail but relies on both normal and defective samples for training, which may not be feasible in medical device datasets.

RAG-PaDiM: Kim et al. [38] extend PaDiM [39] by incorporating Attention U-Nets [40] to generate patch embeddings. These are modelled using multivariate Gaussian distributions, and anomalies are detected using Mahalanobis distance. While innovative, RAG-PaDiM requires labelled defective samples to initialise attention layers, exceeding the limits of small, defect-sparse datasets.

D. LITERATURE REVIEW SUMMARY

In summary, existing methods for anomaly detection have advanced considerably, but most target general-purpose datasets (MNIST, CIFAR-10, ImageNet) rather than manufacturing inspection. These datasets differ substantially from regulated manufacturing images, which are high-resolution, low-complexity, and resource-constrained.

For this reason, we selected four representative architectures—Vanilla Autoencoders, MOCCA, CPCAE, and RAG-PaDiM—as baselines. Each provides valuable insight:

- Vanilla Autoencoders: simple, low-complexity, usable in unsupervised or supervised thresholding modes.
- MOCCA: improved performance but computationally heavy.
- CPCAE: effective for high-resolution data but reliant on defect samples.
- RAG-PaDiM: innovative embedding distributions but requires supervised initialisation.

These limitations underscore the need for new approaches tailored to medical device inspection, where datasets are small, imbalanced, and constrained by regulatory and hardware realities.

III. PROPOSED ARCHITECTURE and METHODS:

We propose two architectures with comparable performance, both of which can be trained in unsupervised mode, using only normal samples, or in supervised mode, where a small number of defective samples are used to optimise the anomaly threshold selection.

These architectures draw inspiration from state-of-the-art deep anomaly detection models while tailoring performance to the specific characteristics of images used in the inspection of medical devices during manufacturing. Such images are typically high-resolution, and downsizing them often results in a significant loss of performance. However, practical hardware limitations in manufacturing inspection environments restrict the maximum image size that can be processed efficiently.

To address this, both architectures partially adopt a patch-based processing strategy, as seen in RAG-PaDiM and CPCAE, to handle high-resolution images. Performance is further enhanced by exploiting the characteristics of To address this, both architectures partially adopt a patch-based processing strategy, as seen in RAG-PaDiM and CPCAE, to handle high-resolution images. Performance is further enhanced by exploiting the characteristics of medical device imagery. Given the strict regulatory environment, image acquisition systems are designed to minimise and control environmental variability, such as part positioning. Furthermore, while defective samples are limited, their nature is generally well understood and characterised through risk assessments and experimentation. This enables accurate localisation of likely defect regions and allows for the generation of attention masks, which define variable regions of interest (ROIs) where defects are expected. Attention-Mask functions are domain specific and detail implementation will vary from dataset to dataset, but we anticipate that attention-masks required to locate defective areas within medical device product would share similar requirements and can be addressed with the use of gradient-based edge detector such as Sobel operator [43], in our case by dynamically detecting the edges of the pouch transition that defines a horizontal line across the pouch and setting a fix size as the image acquisition systems used in manufacturing ensures minimal degree of movement, tilt or magnification. Consequently, our method replaces the conventional use of fixed patches spanning the entire image with an array of mask functions that output ROI coordinates [(x0, y0), (x1, y1)] for each patch i of each image j:

$$F_i(Image_j) = Attention - Patch_{ij}$$

Equation 1

As illustrated in Figure 2, both architectures are based on a Convolutional Autoencoder with four latent layers. The autoencoder is trained to reconstruct each input Attention-$Patch_{ij}$ in unsupervised mode, using only normal samples, with mean squared error (MSE) as the loss function.

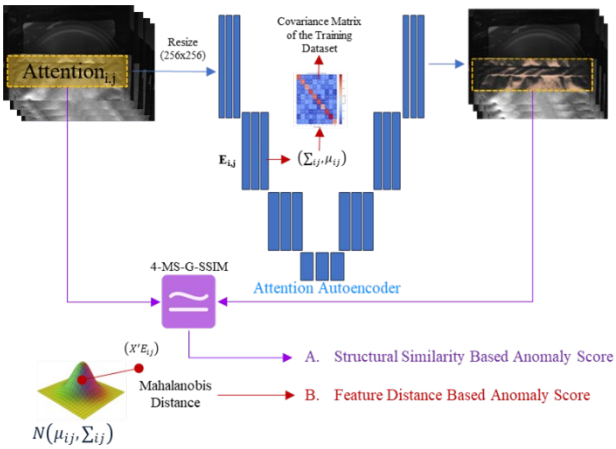

Figure 2 ***Attention Autoencoder with Anomaly Detection Score methods***

A. Structural Similarity Based Anomaly Score

In the first approach, once the backbone Attention Autoencoder has been trained and reconstructed each image in the training set, anomaly scores are computed by comparing the structural similarity between the original and reconstructed images. For this, we employ a variant of the Structural Similarity Index (SSIM) originally introduced by Wang et al. [44].

Unlike pixel-wise metrics such as MSE or PSNR, SSIM measures similarity by comparing luminance, contrast, and structural information. Formally, SSIM between two image patches x and y is given by:

$$SSIM(x,y) = \frac{(2\mu_x\mu_y + C_1)(2\sigma_{xy} + C_2)}{(\mu_x^2 + \mu_y^2 + C_1)(\mu_x^2 + \mu_y^2 + C_2)}$$

Equation 2

Where μ_x, μ_y are the local means of x and y, μ_x^2, μ_y^2 , their variances, σ_{xy} the covariance and C_1, C_2 are the constants to stabilise the division.

Building on this formulation, Renieblas et al. [46] proposed a family of extended SSIM metrics specifically designed for radiological image analysis, including **4-MS-G-SSIM** which we adopt in our method. This variant combines four components:

1. Luminance similarity
2. Contrast similarity
3. Structural similarity
4. Gradient similarity (to capture edge information)

and integrates a multi-scale (MS) evaluation, enabling similarity assessment across different resolutions.

Thus, **4-MS-G-SSIM** extends the original SSIM by introducing gradient information and multi-scale analysis, improving sensitivity to structural distortions and yielding more discriminative anomaly scores.

Once anomaly scores $\mathcal{L}_{ij}$ are obtained for each patch **i** of each image **j** in the training dataset, the **Unsupervised anomaly threshold** $T_{Unsupervised}$ is determined using only the defect-free (class 0) samples as:

$$T_{Unsupervised} = \mu_{norlam} + 2\sigma_{normal}$$

Equation 3

were

$$\mu_{norlam} = \frac{1}{N_0}\sum_{i=1}^{N_0}\mathcal{L}_i$$

Equation 4

and

$$\sigma_{normal} = \sqrt{\frac{1}{N_0 - 1}\sum_{i=1}^{N_0}(\mathcal{L}_i - \mu_{norlam})^2}$$

Equation 5

With $\{\mathcal{L}_i\}_{i=1}^{N_0}$ denoting the anomaly scores of the N_0 defect-free samples.

Under the assumption of approximate normality, this threshold encompasses about 97.7% of the normal data distribution, so values beyond this limit are flagged as potential defects.

We evaluated three methods for determining the decision threshold on anomaly scores obtained from defect-free samples. The first was based on Extreme Value Theory (EVT), which models the tail of the score distribution to set thresholds at controlled false-positive rates. While EVT is widely applied in anomaly detection, it requires a sufficiently large pool of normal samples to yield a stable tail fit. In our case, the dataset contained only 382 normal scores, which is below the minimum typically recommended for reliable EVT modelling, and the method was therefore discarded. The second method relied on selecting the empirical 95th percentile of the score distribution, while the third applied the mean plus two standard deviations rule as described in Equation 3. As reported in Table 13-Appendix C, both of these latter methods produced broadly similar thresholds and comparable performance. However, the μ+2σ rule was ultimately selected, as it provided slightly better accuracy for the selected methodology 4-MS-G-SSIM, and offered clearer interpretability for deployment in regulated manufacturing environments, where statistical transparency and explainability are critical.

To exploit the additional information from the (typically small) set of defective samples available in medical device datasets, a **Supervised threshold** $T_{Supervised}$ can also be defined by maximising the classification accuracy over all possible thresholds on the training set:

$$T_{Supervised} = \underset{T\in[0,1]}{\operatorname{argmax}} \frac{1}{N}\sum_{i=1}^{N} 1\big((\mathcal{L}_i \geq T) \Leftrightarrow (y_i = 1)\big)$$

Equation 6

where **N** is the number of training samples, and $\mathbf{y_i \in \{0,1\}}$ indicates its ground-truth class label (0 = defect-free, 1 = defective). This formulation explicitly leverages both classes to identify the threshold that maximises classification performance on the training data.

B. Feature Distance Based Anomaly Score

The second method also uses the backbone Attention Autoencoder but follows the design principles of MOCCA and RAG-PaDiM. Instead of relying on reconstructed images, this approach operates directly on latent features to compute anomaly scores. Specifically, the Mahalanobis distance is calculated between the embeddings E_{ij} from layer 2 of the autoencoder and the corresponding multivariate Gaussian distribution $N\left(\mu_{ij}, \sum_{ij}\right)$. learned during training:

$$M(x_{ij}) = \sqrt{(E_{ij} - \mu_{ij})^T \sum_{ij}^{-1} (E_{ij} - \mu_{ij})}$$

Equation 7

To mitigate hardware constraints while retaining acceptable performance in manufacturing settings, we reduce computational complexity by randomly selecting 1000 features from layer 2.

As in the previous method, thresholds can be determined in unsupervised mode (Equation 3) or supervised mode (Equation 6).

IV. EXPERIMENTAL METHODOLOGY

The aim of the experiments is to evaluate the performance of the proposed architectures and methods against both a simple deep anomaly detection baseline—the Vanilla Autoencoder—and more advanced models, including MOCCA, CPCAE, and RAG-PaDiM. In addition to benchmarking, the experiments are designed to empirically justify several of the key design choices underpinning our architectures. All evaluations are conducted under realistic manufacturing conditions, with restricted training hardware, comparable optimisation efforts, and a dataset of manufacturing images containing only a small number of defective samples, making it particularly suitable for supervised approaches.

A. Hardware Configuration and Code Repository

The hardware used for the experiments reflects typical industry-level setups employed in the development of manufacturing applications. Although no detailed study was carried out to quantify the impact of hardware limitations on training performance, constraints on computing capacity were introduced deliberately. The primary objective of this research is to design deep anomaly detection solutions that can be deployed within standard manufacturing environments, and based on our experience, we consider the selected hardware representative of such conditions. These environments often operate with limited resources, as manufacturing applications are typically bespoke and do not generally justify substantial investment in high-end infrastructure.

All experiments were conducted on a workstation with the following configuration:

- **CPU**: Intel Core™ i7.
- **GPU 1**: RTX4080, 16GB, 640 Tensor Cores, 9728 CUDA Cores.
- **RAM**: 64GB DDR4, 2400MHz.
- **Hard Drive**: SSD 1TB, 7,000 MB/s.

B. Image Data Set

Experiments were conducted using the publicly available Surface Seal Image (SSI) Dataset of Sterile Barrier Packaging [3], which contains two classes: normal samples and defective samples. This dataset reflects typical manufacturing conditions in terms of image quality and composition and provides multiple subsets with varying degrees of class imbalance, ranging from 1% to 50% defective samples.

The primary objective of our proposed architecture is to achieve optimal performance in the unsupervised setting, that is, when trained exclusively with defect-free samples. However, our methodology also accommodates the use of a limited number of defective samples for anomaly threshold selection, reflecting the practical reality of medical device datasets, where only a small proportion of defective samples are typically available. The SSI dataset therefore offers an appropriate basis for experimentation under both conditions.

As highlighted by Zanon et al. [2], in collaboration with industry partners, defect rates in highly regulated manufacturing industries can be as low as 0.1%. Given typical production volumes, assembling ~1,000 samples with a 50% defect rate could require up to 2.5 years of production, making such datasets impractical. To simulate realistic industrial conditions, we adopted two training and cross-validation subset 'Partial-10', containing 10% defective samples, used during the development and testing of the architecture; and 'Partial-1', containing 1% defective samples, used to challenge experimentation.

In addition to these training and cross-validation subsets, a balanced dataset ('Test-split') was used exclusively for final testing. This subset was not involved in architectural design decisions, ensuring maximum generalisation potential and

objective evaluation. Table 1 summarises the dataset configurations employed in our experiments.

Table 1. Dataset Sub-Sets

Sub-Set Name	*Description*	Image quantities		
		Total	*Good*	*Defects*
'Partial-10'	Training and Cross-Validation	424	382	42
'Partial-1'	Training and Cross-Validation	424	420	4
'Test-split'	Testing	360	180	180

It is important to note that while the selected subsets enable the evaluation of supervised approaches, they impose limitations on unsupervised methods. Based on typical manufacturing volumes [2], a six-month data collection period could yield more than 50,000 normal samples, which would be expected to significantly improve the performance of unsupervised models trained solely on defect-free data. At present, however, no publicly available datasets of this scale meet the requirements of our research. Although this limitation does not preclude meaningful experimentation, future studies should consider repeating these evaluations with larger normal-only datasets.

Figure 3 illustrates a representative image from the 'Partial-10' training and cross-validation subset.

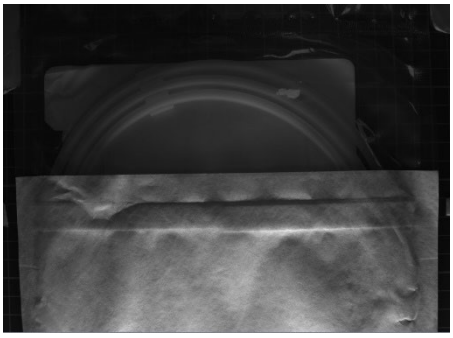

Figure 3 ***SSI dataset example***

C. Model Implementation and Optimisation approach

Scripting: Code is available in repository https://github.com/JulioZanon/Structural-Similarity-and-Feature-Distance-Based-Deep-Anomaly-Detection-for-High-Resolution-Images.

Image Pre-processing: No preprocessing of images is carried out other than resizing images to 256x256x3 to overcome hardware performance constraints.

Optimisation approach:

Hyperparameter tuning techniques included Bayesian optimiser and grid searches. Due to hardware limitations, batch sizes were limited to low values. To produce consistent benchmarking indicators, we omitted the used of k-folds and instead randomly split the training set into Training and Xval splits (70% / 30%) with a fix seed.

V. EXPERIMENTAL RESULTS

The first set of experiments, trained with the 'Partial-10' subset, was used to establish a baseline for the development of our methodology. For this purpose, we implemented and trained both basic and advanced deep anomaly detection architectures identified in the literature, including Vanilla Autoencoders and more recent models such as MOCCA, CPCAE, and RAG-PaDiM. These experiments also introduced the use of attention-patch functions within the Autoencoder.

It should be noted that the original source code for these architectures was not publicly available. Our implementations followed the architectural descriptions provided in the publications as closely as possible. However, due to incomplete implementation details and potential differences in preprocessing or training setups, we cannot guarantee exact reproduction of the reported results. For this reason, the results presented for MOCCA, CPCAE, PaDiM, AG-PaDiM, and RAG-PaDiM should be interpreted as reference benchmarks rather than strict replications of the original methods. This framing highlights the reproducibility challenges in anomaly detection research, and underscores the importance of open-source availability for fair evaluation.

Table 2. Benchmark Study Trained with "partial-10" and results obtained from the Test subset

Model	AUC	ACC	P	R	F1
MOCCA	0.724	0.694	0.639	0.894	0.745
CPCAE	0.817	0.742	0.664	**0.978**	**0.791**
Padim	0.720	0.664	0.620	0.844	0.716
AG-Padim	0.664	0.598	1.000	0.748	0.664
RAG-Padim	0.500	0.500	1.000	0.667	0.500
Vanilla AE (4 Layers)	0.614	0.614	**0.936**	0.244	0.388
AAE-MSE	**0.881**	**0.708**	0.931	0.450	0.607

From these results, we inferred that the Vanilla Autoencoder, when enhanced with attention-patch functions (Referred to as AAE), demonstrated strong potential for performance improvement. However, recall remained very low, indicating that the autoencoder with MSE anomaly score was biased toward the normal class on which it was trained. In the context of quality inspections in highly regulated industries, this finding is critical, as missed defect detections can have serious implications, underscoring the need for methods that preserve recall while maintaining robustness in highly regulated inspection environments.

The optimisation of the vanilla autoencoder to determine a 4-layers architecture was carried out by setting a 2-steps optimisation script with a Bayesian optimiser and the hyperparameters in Table 11 and Table 12 in Appendix B.

a) Structural Similarity-Based Scoring

In the second set of experiments, we evaluated different variants of the SSIM index family for anomaly scoring in our first proposed approach. These included metrics originally proposed by Li and Bovik [45] and later extended by Renieblas et al. [46]. All models were trained on the "Partial-10" subset, with anomaly thresholds determined in supervised mode.

Table 3. Attention AE Anomaly Detection with Supervised Threshold and results obtained from the Test subset

Model	AUC	ACC	P	R	F1
MSE	0.881	0.708	0.931	0.450	0.607
SSIM	0.930	0.825	0.838	0.806	0.822
PSNR	0.866	0.744	0.855	0.589	0.697
MAE	0.915	0.781	0.885	0.644	0.746
MS-SSIM	0.922	0.808	0.840	0.761	0.799
4-SSIM	0.969	0.867	0.817	**0.944**	0.876
4-MS-SSIM	**0.977**	**0.931**	**0.938**	0.922	**0.930**
4-G-SSIM	0.530	0.500	0.500	0.028	0.053
4-MS-G-SSIM	0.843	0.700	0.853	0.483	0.617

Among these, **4-MS-SSIM** achieved the best overall balance of sensitivity and robustness, corroborating the findings reported in [45].

It is noteworthy that the gradient-extended variant (AAE-4-G-SSIM) degraded markedly, with accuracy dropping to 0.530. The 'G' denotes the inclusion of a gradient similarity term, which measures consistency of local edge information between the input and reconstruction. While this component enhances sensitivity to structural distortions, in our experiments it proved overly sensitive to small reconstruction artefacts in defect-free samples, leading to a high false positive rate. By contrast, the multi-scale variants (AAE-4-MS-SSIM and AAE-4-MS-G-SSIM) stabilised this sensitivity by averaging across resolutions, yielding robust improvements. This highlights the importance of multi-scale integration when incorporating gradient-based similarity

As an additional experiment, we investigated whether performance could be improved by replacing the single-score thresholding strategy with a supervised machine learning model that integrates multiple descriptors. Specifically, we aggregated anomaly scores from the SSIM variants and combined them with GLCM-based texture features, originally proposed by Haralick et al. [47], which capture second-order statistical dependencies of pixel intensities. These feature vectors were then used to train Random Forest (RF), Support Vector Machine (SVM), and Logistic Regression (LR) classifiers to optimise decision boundaries.

Table 4. ML Threshold Selection with AEE (4-MS-SSIM)

Model	ACC	P	R	F1
RF	0.914	**0.916**	**0.911**	**0.914**
SVM	0.900	0.891	**0.911**	0.901
LR	**0.956**	0.717	0.819	0.842

Although these supervised models achieved competitive results, they did not outperform the simpler supervised thresholding of **4-MS-SSIM**. This suggests that the added complexity of integrating heterogeneous descriptors offers little practical benefit for this dataset.

Finally, we compared unsupervised thresholding of the 4-MS-SSIM method with supervised thresholding trained on two subsets: the "Partial-10" split, containing 42 defective samples (10% of the dataset), and the "Partial-1" split, containing only 4 defective samples (1% of the dataset).

Table 5. AEE (4-MS-SSIM) Supervised vs Unsupervised Threshold and results obtained from the Test subset

Model	ACC	P	R	F1
Supervised (Trained Partial-10)	**0.931**	0.938	0.922	**0.930**
Supervised (Trained Partial-1)	0.803	**0.991**	0.611	0.756
Unsupervised	0.903	0.847	**0.983**	0.910

As expected, supervised thresholding—when trained with an abundant number of defective samples (10% or above)—delivered slightly higher accuracy and precision. However, the gain was marginal, reinforcing the viability of our architecture in a fully unsupervised setting, which is particularly advantageous in domains where defective samples are scarce. More importantly, while recall was very poor when the supervised model was trained with only 1% defective samples, recall remained high for the other two configurations (0.922 for supervised with 10% and 0.983 for unsupervised). This demonstrates that both approaches can be reliably deployed for defect inspection in highly regulated manufacturing processes.

b) Feature-Distance-Based Scoring

The third set of experiments focused on the second proposed method, evaluating strategies for extracting latent features and computing anomaly scores. Again, the 'Partial-10' subset was used, with thresholds set in supervised mode and results reported on the Training subset to avoid overfitting.

Given hardware limitations, several dimensionality reduction methods were tested, including Principal Component Analysis (PCA) with a variable retention of components to capture 95% of variation, Independent Component Analysis (ICA), and random feature drop (initially reducing to 500 features). Two approaches were then evaluated for anomaly scoring: K-Means clustering and Mahalanobis distance.

Table 6. All Features in Covariance Matrix on Training subset

Model	AUC	ACC	P	R	F1
PCA-K-Means	0.663	0.617	0.566	0.994	0.722
PCA-M	0.543	0.500	0.500	1.000	0.667
K-Means	0.446	0.519	0.516	0.633	0.569
ICA-M	0.463	0.492	0.200	0.006	0.011
Random Drop – K-Means	0.589	0.589	0.554	0.906	0.688
Random Drop – M	**0.909**	**0.836**	**0.789**	**0.917**	**0.848**

From this analysis, we concluded that random feature drop combined with Mahalanobis distance provided the most effective balance of computational efficiency and detection accuracy.

We justify random feature reduction through an intuition related to the Johnson–Lindenstrauss lemma: high-dimensional embeddings can be projected into much lower dimensions while approximately preserving pairwise distances. Although our reduction is based on random feature selection rather than dense random projections, the same principle applies: provided the reduced dimension remains sufficiently large, anomaly-relevant distances are preserved with high probability. This perspective helps explain why our method maintains discriminative power despite aggressive dimensionality reduction

It is worth noting that by aggressively reducing feature dimensionality, we alleviate the need for shrinkage-based covariance regularisation, as the reduced covariance matrices are well-conditioned and can be reliably estimated with the available normal samples

c) Feature Extraction Ablation Study

An ablation study was then conducted to determine the optimal degree of feature reduction using random drop, and to evaluate whether features extracted from specific autoencoder layers outperform those extracted from all layers. This study was again carried out using only the images in the training dataset to avoid overfitting. Results are provided in Appendix A – Table 9 and Table 10, showing that a random feature selection of 500 to 1000 features, from Layer 1 or layer 2, performed similarly, achieving the best trade-off between computational efficiency and performance with 500 randomly selected features from layer 2.

To confirm these findings, we repeated the experiments using features from Layers 1 and 2, applying both random drop and PCA, with training on the 'Partial-10' subset and thresholds set in unsupervised mode. These results are again obtained on the training dataset to avoid overfitting.

Table 7. Mahalanobis distance on Training subset

Model	AUC	ACC	P	R	F1
PCA-Layer1	0.694	0.500	---	---	---
PCA-Layer2	0.643	0.503	1.000	0.006	0.011
RandomDrop-Layer1	0.910	0.850	**0.812**	0.911	0.859
RandomDrop-Layer2	**0.920**	**0.861**	0.801	**0.961**	**0.874**

This confirmed that features in both individual layers, 1 and 2, offer similar anomaly detection capabilities, achieving an accuracy of 0.850 and 0.861 respectively against training data, and outperforming any of the methods in Table 6, using all layers, as report.

Finally, we compared supervised versus unsupervised thresholding for random drop in layer 2, using the Test subset.

Table 8. RandomDrop-Layer2 Supervised vs Unsupervised Threshold in Test Dataset

Model	ACC	P	R	F1
Supervised	**0.722**	**0.643**	**1.000**	**0.783**
Unsupervised	0.658	0.594	**1.000**	0.745

As expected, supervised thresholding achieved higher accuracy, though still significantly lower than the performance observed on the Training subset. To better understand this gap, we examined Figure 4, which depicts the distribution of Mahalanobis distances for both the Training and Test subset.

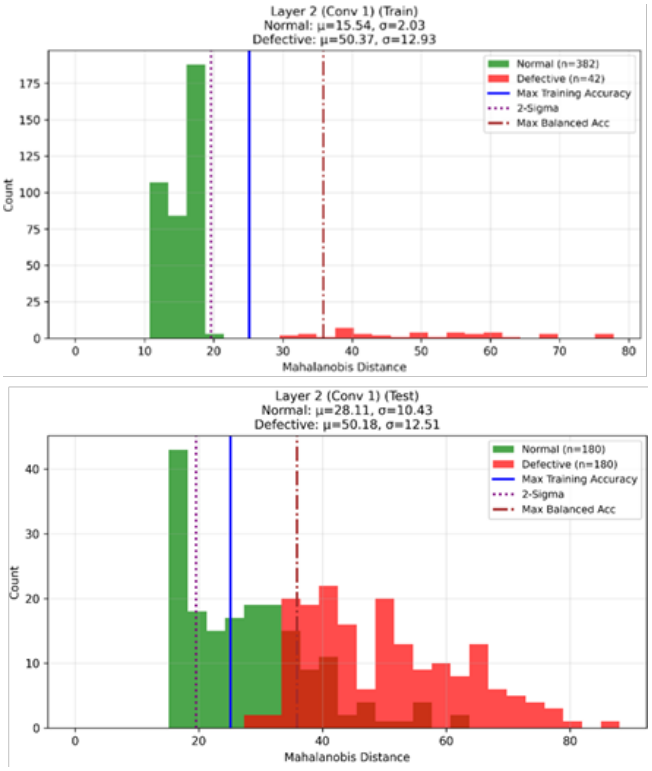

Figure 4 **Histogram of Mahalanobis distances for Training and Test datasets**

As observed, the distributions of defective samples were highly consistent across datasets, with nearly identical means (50.37 in Training vs. 50.18 in Test) and similar standard deviations (12.93 vs. 12.51). In contrast, the distributions of normal samples diverged markedly: the Training dataset exhibited a narrow spread (standard deviation = 2.03), whereas the Test dataset showed a much broader spread (standard deviation = 10.43).

These findings suggest that the backbone autoencoder strongly overfitted to the training data. This was intentional by design: the model was developed to overfit on the normal class, which is typically abundant, so that it generalises poorly on defective samples and produces higher anomaly scores. In practice, this approach requires a very large pool of normal images to ensure that the learned representation captures the true variability of the defect-free class. In our experiments, however, the number of normal samples in training (382) was modest compared to the number in the Test set (180), leading to higher variance in unseen normal images. This mismatch reduced precision by causing false positives. We therefore expect that with much larger quantities of defect-free samples—more representative of the real distribution—the model would better approximate the normal class and yield the intended effect of discriminating defects without penalising unseen but valid normal samples.

As a result of the relatively low number of testing samples, distinguishing anomalous from normal features became more difficult, lowering generalisation performance and, in particular, precision. In practical terms, this would translate into an inspection system prone to generating high levels of false scrap.

On the other hand, the method's sensitivity to variations in image composition could be leveraged in supervisory contexts. While less suitable for automated online edge inspection, it may provide significant value in post-production analysis, where shifts in feature distributions could be monitored to detect or even predict emerging manufacturing issues.

VI. DISCUSSIONS

Our baseline evaluation demonstrated that while MOCCA, CPCAE, PaDiM, AG-PaDiM, and RAG-PaDiM are recent and innovative, our re-implementations did not achieve competitive results. Performance was frequently comparable to a Vanilla Autoencoder. Since source code for these models was unavailable, our reproductions relied on textual descriptions, leaving scope for discrepancies in pre-processing, hyperparameters, and training schedules. For this reason, we report them as reference benchmarks rather than strict replications. This distinction underscores reproducibility challenges that persist in anomaly detection research.

The introduction of attention-mask functions significantly improved performance, increasing Vanilla AE accuracy from 0.614 to 0.708. Although designed for the SSI dataset, attention masks are likely generalisable to other medical device inspection tasks, where parts are consistently positioned and defects occur in predictable regions. Extending this approach to full-image attention overlays with adaptive loss weighting may further improve generalisation and enable detection of anomalies outside predefined ROIs.

The **structural similarity–based method** (4-MS-SSIM) achieved strong results on the SSI dataset: 0.903 accuracy with unsupervised thresholding and 0.931 when trained with 10% defective samples. However, supervised training with only 1% defects reduced accuracy to 0.803 and recall to 0.611, a configuration that would risk unacceptable defect escape rates in regulated manufacturing. Importantly, all results surpassed benchmark baselines, demonstrating the value of our approach when applied in unsupervised mode or with sufficient defective training samples. Early experiments also showed that directly training the autoencoder with SSIM as the loss degraded anomaly separability. We attribute this to the distinct roles of the loss and scoring functions: MSE promotes consistent reconstruction of normality, while SSIM provides perceptual discrimination when applied post hoc.

The **feature distance–based method**, inspired by MOCCA and RAG-PaDiM, was redesigned to address industrial hardware constraints. By reducing ~1,000,000 latent features to 500 randomly selected features from Layer 2, it achieved accuracy of 0.722 (supervised) and 0.658

(unsupervised). Recall remained perfect (1.0) in both cases, but precision was low, indicating high false-scrap rates—an important limitation in medical device manufacturing. Analysis of Mahalanobis-score distributions revealed that the method is highly sensitive to changes in the normal class, a symptom of backbone overfitting. While problematic for inline edge inspection, this sensitivity is advantageous for supervisory applications, where feature distributions can be tracked post-production to monitor process drift and predict potential manufacturing issues. This aligns with forthcoming EU AI Act requirements for deployed-model monitoring.

Taken together, the results suggest a **complementary deployment strategy**. The structural similarity–based method is best suited for real-time, edge deployment on production lines, where low computational overhead and high recall are critical. The feature distance–based method is more suitable for cloud-level supervisory monitoring, where compact latent features can be stored inexpensively and analysed retrospectively. Because both approaches share the same attention-based autoencoder backbone, they can operate jointly: the first ensuring inline defect detection, and the second enabling long-term monitoring of feature distributions.

To illustrate these complementary roles, Figure 5 presents a practical deployment framework. The SSIM-based method operates at the edge, embedded in production-floor equipment to provide real-time, high-recall defect detection. In parallel, the feature-distance method processes randomly selected latent features in a cloud environment, enabling supervisory batch-level monitoring, detection of process drift, and compliance with emerging regulatory expectations for post-deployment monitoring. Together, these layers form a dual-purpose inspection system that balances immediate operational requirements with long-term governance and regulatory readiness.

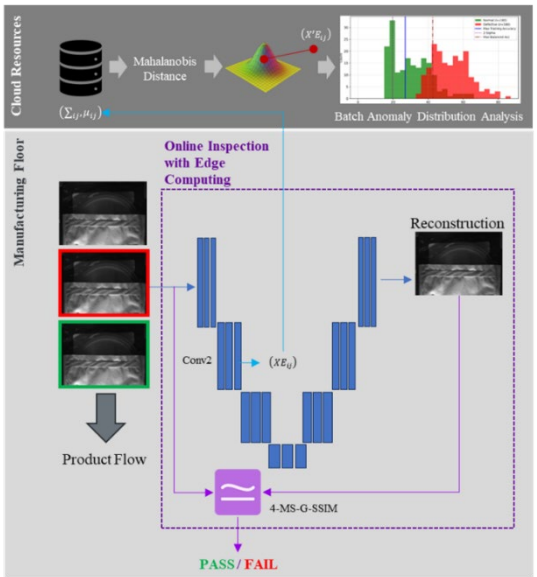

Figure 5 ***Practical deployment framework for the proposed anomaly detection methods.***

The alignment of our methods with evolving regulatory expectations is particularly important. Under the EU Artificial Intelligence (AI) Act [49], AI systems used in the manufacture of Class III medical devices are classified as high-risk systems and are therefore subject to stringent obligations covering risk management, data governance, explainability, and post-deployment monitoring. Similarly, the U.S. FDA has issued draft guidance [48] highlighting the importance of transparency, documentation of model development, and continuous lifecycle surveillance of AI-enabled manufacturing systems.

Within this context, our two complementary approaches map naturally to these obligations, particularly model monitory and explainability. The SSIM-based method offers transparency and explainability through similarity scores that are readily interpretable, directly supporting traceability and human oversight requirements. The feature-distance method, while less precise for inline deployment, provides continuous monitoring of distributional shifts, which aligns with emerging post-market surveillance requirements under the EU AI Act and explainability by retaining a low-weight representation of the image in the form of a reduce feature set for future investigations to assist the explainability of past results. Together, these methods provide not only operational advantages but also a practical foundation for regulatory acceptance in high-risk industrial environments.

VII. CONCLUSIONS AND FUTURE WORK

In this work, we proposed and evaluated two attention-guided autoencoder architectures for deep anomaly detection in medical device manufacturing. Both methods address the challenges of small, imbalanced datasets and constrained hardware, providing practical solutions for regulated industrial environments.

1. **Structural similarity–based anomaly scoring**: Using the 4-MS-SSIM index, this method achieved superior performance on the SSI dataset (0.903 unsupervised; 0.931 supervised with 10% defects). Its robustness and efficiency make it well suited for inline, edge-based deployment in production.
2. **Feature distance–based anomaly scoring**: Leveraging Mahalanobis distance on 500 randomly reduced features from Layer 2, this method balances feasibility and discrimination while reducing storage cost. Although precision was limited, its high sensitivity to distributional change makes it promising for supervisory post-production monitoring and model governance.

Both unsupervised and supervised thresholding strategies were evaluated. While supervised tuning provided marginal gains when sufficient defective samples were available, unsupervised thresholding proved highly competitive and

remains preferable for generalisation. Importantly, our methods consistently outperformed re-implemented baselines (MOCCA, CPCAE, PaDiM, AG-PaDiM, RAG-PaDiM) under controlled, hardware-constrained conditions, reinforcing the importance of open, reproducible benchmarks.

Future work will extend this research along several directions:

- We will develop full-image attention overlays with weighted loss functions in order to capture defects beyond predefined regions of interest and improve generalisation across varying defect locations.
- We will explore hybrid training objectives that combine MSE and SSIM, enabling the reconstruction process to benefit from both pixel-level fidelity and perceptual sensitivity to structural distortions.
- We will refine the feature reduction strategy by replacing random selection with principled methods, such as attention-based ranking of latent features or sparsity constraints, to retain only the most discriminative and informative representations.
- We will validate our approaches on larger, industry-scale datasets containing predominantly normal samples, as these are essential to fully realise our intentional design of overfitting on the normal class. Such datasets would better capture the inherent variability of defect-free products, allowing the autoencoder to generalise more robustly across unseen normal samples while still producing high anomaly scores for defective ones.
- We will conduct broader benchmarking against external datasets from other domains, providing a more comprehensive evaluation of the generalisability and robustness of the proposed architectures.
- We will develop a strategy with a model release dossier and qualification protocols to meet requirements under the EU AI Act.

In conclusion, the proposed architectures demonstrate strong potential for anomaly detection in highly regulated manufacturing. By combining edge-ready structural similarity scoring with supervisory feature-based monitoring, they provide a practical pathway toward dual-purpose inspection systems that meet both operational requirements and emerging regulatory standards. Together, these directions will enhance the technical performance, robustness, and regulatory readiness of deep anomaly detection models for industrial deployment.

Beyond their technical contributions, the proposed architectures anticipate regulatory requirements for AI in medical device manufacturing. By emphasising interpretability (via structural similarity scores), robustness in small-data regimes, and inherent monitoring of feature distributions, they provide practical mechanisms for addressing compliance obligations defined under the EU AI Act [49] and forthcoming FDA guidance on AI in manufacturing [48]. This dual orientation—towards operational performance and compliance—reinforces their suitability for deployment in safety-critical and highly regulated environments.

REFERENCES

[1] J. Rodríguez-Pérez, "Human Error Reduction in Manufacturing", 2023, American Society for Quality, Quality Press, Milwaukee 53203, ISBN: 978-1-63694-090-8

[2] J. Zanon Diaz, M.A. Farooq, P. Corcoran, "Automatic inspection of seal integrity in sterile barrier packaging: a deep learning approach", 2024, IEEE Access 22904–22927, DOI:10.1109/ACCESS.2023.3348779.

[3] J. Zanon Diaz, P. Corcoran, "Surface seal image dataset of sterile barrier packaging", 2024, Science Direct - Data in Brief, Vol. 57, 2352-3409, arXiv, DOI:10.1016/j.dib.2024.110996.

[4] F.V. Massoli, F. Falchi, A.Kantarci, S. Akti, H.K. Ekenel, and G. Amato, "MOCCA: Multilayer One-Class Classification for Anomaly Detection". 2022, IEEE Transaction on Neural Networks and Learning Systems, vol. 33, no. 6, 2022, pp. 2313–2323. DOI :10.1109/TNNLS.2021.3130074.

[5] T. Daniel, T. Kurutach, and A. Tamar, "Deep Variational Semi-Supervised Novelty Detection", 2019, DOI:10.48550/arXiv.1911.04971.

[6] I. Kim, Y. Jeon, J.W. Kang and J. Gwak, "RAG-PaDiM: Residual Attention Guided PaDiM for Defects Segmentation in Railway Tracks", 2023, Journal of Electrical Engineering & Technology, no. 18(2), pp. 1429–1438. DOI:10.1007/s42835-022-01346-2.

[7] J. Saeedi, and A. Giusti, A., "Semi-supervised visual anomaly detection based on convolutional and transfer learning", 2023, Machine Learning with Applications, no.11, pp.100451. DOI:10.1016/j.mlwa.2023.100451.

[8] Q. Yuan and Z. Zuo, "Research on the Performance of different Convolutional Neural Network Models on small Datasets," 2022, International Conference on Machine Learning and Intelligent Systems Engineering (MLISE), Guangzhou, , pp. 57-62, DOI:10.1109/MLISE57402.2022.00019.

[9] S. Bozinovski and A. Fulgosi, "The influence of pattern similarity and transfer learning upon training of a base perceptron B2" (original in Croatian), 1976, Proceedings of Symposium Informatica 3-121-5.

[10] K. Weiss, T.M. Khoshgoftaar and D. Wang, "A survey of transfer learning", 2016, Journal of Big Data 3, 9.

[11] DS. Terzi, "Effect of Different Weight Initialization Strategies on Transfer Learning for Plant Disease Detection.", 2024, Plant Pathology, vol. 73, no. 9, pp. 2325–2343, DOI:10.1111/ppa.13997.

[12] N. Tajbakhsh, J. Y. Shin, S. R. Gurudu, R. T. Hurst, C. B. Kendall, M. B. Gotway, and J. Liang, ''Convolutional neural networks for medical image analysis: Full training or fine tuning?'' IEEE Trans. Med. Imag., vol. 35, no. 5, pp. 1299–1312, May 2016, DOI:10.1109/TMI.2016.2535302.

[13] D. R. Clymer, J. Long, C. Latona, S. Akhavan, P. LeDuc, and J. Cagan, ''Applying machine learning methods toward classification based on small datasets: Application to shoulder labral tears,'' J. Eng. Sci. Med. Diag. Therapy, vol. 3, no. 1, p. 1, Feb. 2020, DOI:10.1115/1.4044645.

[14] N. Arunkumar, M. A. Mohammed, S. A. Mostafa, D. A. Ibrahim, J. J. P. C. Rodrigues, and V. H. C. de Albuquerque, ''Fully automatic model-based segmentation and classification approach for MRI brain tumor using artificial neural networks'', 2022, Concurrency Comput., Pract. Exper., vol. 32, no. 1, pp. e496, DOI:10.1002/cpe.4962.

[15] A. Shaban, S. Bansal, Z. Liu, I. Essa, and B. Boots, ''One-shot learning for semantic segmentation,'' 2017, DOI:1709.03410.

[16] Y. Bao, K. Song, J. Liu, Y.Wang, Y. Yan, H. Yu, and X. Li, ''Triplet-graph reasoning network for few-shot metal generic surface defect segmentation'', 2021, IEEE Trans. Instrum. Meas., vol. 70, no. 5011111, DOI:10.1109/TIM.2021.3083561.

[17] A. Krizhevsky, I. Sutskever, and G. E. Hinton, ''ImageNet classification with deep convolutional neural networks'', 2017, Commun. ACM, vol. 60, no. 6, pp. 84–90, DOI: 10.1145/3065386.

[18] Z. Eaton-Rosen, F. Bragman, S. Ourselin, and M. J. Cardoso, ''Improving data augmentation for medical image segmentation'', 2018, in Proc. 1st Conf. Med. Imag. Deep Learn.

[19] G. Zhang, K. Cui, T.-Y. Hung, and S. Lu, ''Defect-GAN: Highfidelity defect synthesis for automated defect inspection'', 2021, in Proc. IEEE Winter Conf. Appl. Comput. Vis. (WACV), pp. 2524–2534.

[20] J. Shi, "Good features to track", In 1994 Proceedings of IEEE conference on computer vision and pattern recognition, pp. 593-600. DOI:10.1109/CVPR.1994.323794.

[21] J. Matas, O. Chum, M. Urban, and T. Pajdla, "Robust wide-baseline stereo from maximally stable extremal regions". 2004, Image and vision computing, Vol.22(10), pp.761-767, DOI:10.1016/j.imavis.2004.02.006.

[22] E. Rosten, and T. Drummond, "Machine learning for high-speed corner detection". 2006, In Computer Vision–ECCV 2006: 9th European Conference on Computer Vision, Part I 9, pp. 430-443. DOI:10.1007/11744023_34.

[23] M. Calonder, V. Lepetit, C. Strecha, and P. Fua, "Brief: Binary robust independent elementary features". 2010, In Computer Vision–ECCV 2010: 11th European Conference on Computer Vision, Proceedings, Part IV 11, pp. 778-792. DOI:10.1007/978-3-642-15561-1_56.

[24] A. Alahi, R. Ortiz, and P. Vandergheynst, "Freak: Fast retina keypoint". 2012, In 2012 IEEE conference on computer vision and pattern recognition, pp. 510-517. DOI:10.1109/CVPR.2012.6247715.

[25] D.G. Lowe. "Object recognition from local scale-invariant features". 1999, In Proceedings of the seventh IEEE international conference on computer vision, Vol. 2, pp. 1150-1157. DOI:10.1109/ICCV.1999.790410.

[26] H. Bay, T. Tuytelaars, and L. Van Gool, L. "SURF: Speeded up robust features". 2006, In Computer Vision–ECCV 2006: 9th European Conference on Computer Vision, Proceedings, Part I 9, pp. 404-417. DOI:10.1007/11744023_32.

[27] E. Simo-Serra, E. Trulls, L. Ferraz, I. Kokkinos, P. Fua, and F. Moreno-Noguer. "Discriminative learning of deep convolutional feature point descriptors". 2015, In Proceedings of the IEEE international conference on computer vision, pp. 118-126. DOI:10.1109/ICCV.2015.22.

[28] K.M Yi, E. Trulls, V. Lepetit, and P. Fua. "Lift: Learned invariant feature transform". 2016, In Computer Vision–ECCV 2016: 14th European Conference, Proceedings, Part VI 14, pp. 467-483. DOI:10.1007/978-3-319-46466-4_28.

[29] J. Revaud, C. De Souza, M. Humenberger, and P. Weinzaepfel. "R2d2: Reliable and repeatable detector and descriptor". 2019, Advances in neural information processing systems, Vol.32. DOI:10.48550/arXiv.1906.06195.

[30] H. Bourlard, and Y. Kamp. "Auto-association by multilayer perceptrons and singular value decomposition". 1988, Biological cybernetics, Vol. 59(4), pp.291-294. DOI:10.1007/bf00332918.

[31] J. Masci, U. Meier, D. Cireşan, and J. Schmidhuber. "Stacked convolutional auto-encoders for hierarchical feature extraction". 2011, In Artificial Neural Networks and Machine Learning–ICANN 2011: 21st International Conference on Artificial Neural Networks, Espoo, Proceedings, Part I 21, pp. 52-59. DOI:10.1007/978-3-642-21735-7_7.

[32] M. Usman, S. Latif, and J. Qadir. "Using deep neural networks for facial expression recognition". 2017, In 2017 13th International Conference on Emerging Technologies (ICET), pp. 1-6. DOI:10.1109/ICET.2017.8281753.

[33] N. Žižakić, and A. Pižurica. "Efficient local image descriptors learned with autoencoders". IEEE Access, Vol. 10, pp.221-235. DOI:10.1109/ACCESS.2021.3138168.

[34] R. Changala, P.K. Yadaw, M. Farooq, M.S. Al Ansari, V.A. Vuyyuru, and S. Muthuperumal. "Advancing Surveillance Systems: Leveraging Sparse Auto Encoder for Enhanced Anomaly Detection in Image Data Security". 2024, In 2024 International Conference on Data Science and Network Security (ICDSNS), pp.1-6. DOI:10.1109/ICDSNS62112.2024.10691001.

[35] S. Kumari, and C. Prabha. "A Comprehensive Review of Deep Anomaly Detection Techniques-An Analysis". 2024, In 2024 IEEE 9th International Conference for Convergence in Technology (I2CT), pp. 1-6. DOI:10.1109/I2CT61223.2024.10543335.

[36] F.V. Massoli, F. Falchi, A. Kantarci, Ş. Akti, H.K. Ekenel, and G. Amato. "MOCCA: Multilayer one-class classification for anomaly detection". 2021, IEEE transactions on neural networks and learning systems, Vol. 33(6), pp. 2313-2323. DOI:10.1109/TNNLS.2021.3130074.

[37] J. Saeedi, and A. Giusti. "Semi-supervised visual anomaly detection based on convolutional autoencoder and transfer learning". 2023,

Machine Learning with Applications, Vol.11, pp.100451. DOI:10.1016/j.mlwa.2023.100451.
[38] I. Kim, Y. Jeon, , J.W. Kang, and J. Gwak. “RAG-PaDiM: residual attention guided PaDiM for defects segmentation in railway tracks”. 2023, Journal of Electrical Engineering & Technology, Vol.18(2), pp.1429-1438. DOI:10.1007/s42835-022-01346-2.
[39] T. Defard, A. Setkov, A. Loesch, and R. Audigier. “Padim: a patch distribution modeling framework for anomaly detection and localization”. 2021, In International Conference on Pattern Recognition, pp. 475-489. DOI:10.1007/978-3-030-68799-1_35.
[40] O. Oktay, J. Schlemper, L.L. Folgoc, M. Lee, M. Heinrich, K. Misawa, K. Mori, S. McDonagh, N.Y, Hammerla, B. Kainz and B. Glocker. “Attention u-net: Learning where to look for the pancreas”, 2018, arXiv preprint DOI:10.48550/arXiv.1804.03999.
[41] N. Otsu, "A Threshold Selection Method from Gray-Level Histograms," in IEEE Transactions on Systems, Man, and Cybernetics, vol. 9, no. 1, pp. 62-66, Jan. 1979,. DOI: 10.1109/TSMC.1979.4310076.
[42] P.C. Mahalanobis, “On the generalised distance in statistics”. 1936, Proceedings of the National Institute of Sciences of India, 2(1), 49–55.
[43] R. C. Gonzalez and R. E. Woods, *Digital Image Processing*, 3rd ed. Upper Saddle River, NJ, USA: Prentice Hall, 2008.
[44] Z. Wang, A. C. Bovik, H. R. Sheikh, and E. P. Simoncelli, “Image quality assessment: from error visibility to structural similarity,” IEEE Transactions on Image Processing, vol. 13, no. 4, pp. 600–612, Apr. 2004.
[45] C. Li and A. C. Bovik, “Content-partitioned structural similarity index for image quality assessment,” Signal Processing: Image Communication, vol. 25, no. 7, pp. 517–526, Aug. 2010, DOI:10.1016/j.image.2010.03.004.
[46] G. P. Renieblas, A. T. Nogués, A. M. González, N. Gómez-León, and E. G. del Castillo, “Structural similarity index family for image quality assessment in radiological images,” Journal of Medical Imaging, vol. 4, no. 3, p. 035501, July 2017. DOI:10.1117/1.JMI.4.3.035501.
[47] Haralick, R. M., Shanmugam, K., & Dinstein, I. (1973). Textural features for image classification. IEEE Transactions on Systems, Man, and Cybernetics, SMC-3(6), 610–621. DOI:10.1109/TSMC.1973.4309314.
[48] U.S. Food and Drug Administration, Considerations for the Use of Artificial Intelligence to Support Regulatory Decision-Making for Drug and Biological Products: Guidance for Industry and Other Interested Parties, Draft Guidance, Jan. 2025. [Online]. Available: https://www.fda.gov/regulatory-information/search-fda-guidance-documents/considerations-use-artificial-intelligence-support-regulatory-decision-making-drug-and-biological.
[49] European Parliament and Council of the European Union, “Regulation (EU) 2024/1684 of the European Parliament and of the Council of 12 July 2024 laying down harmonised rules on artificial intelligence (Artificial Intelligence Act),” Official Journal of the European Union, L 164, Aug. 2024.

Julio Zanon Diaz received his degree in Telecommunications Engineering from the University of Valencia, Spain, in 2000, prior to the Bologna Process reforms that aligned third-level degrees across Europe. He later returned to the University of Valencia to complete a B.Eng. (Hons.) in Electronics in 2017. Since 2001, he has worked as an automation engineer in the automotive and medical device industries, gaining recognised expertise in equipment design, safety, software development, robotics, and machine vision. He is currently a Fellow Engineer at Boston Scientific, where he leads strategies and teams in the development and deployment of advanced manufacturing technologies, with a focus on data science, artificial intelligence, digital twins, and human-centric manufacturing. Mr. Zanon Diaz is also pursuing a Ph.D. in Electrical and Electronic Engineering at the University of Galway, Ireland. His research interests include automated visual inspection using computer vision and deep neural networks in highly regulated manufacturing environments. He previously served as a part-time Adjunct Lecturer with the University of Galway.

George Siogkas (Member, IEEE) is a Senior R&D Consultant and the founder of Irish company CVRLab, specializing in Computer Vision and Machine Learning. He has worked as a R&D Computer Vision engineer for leading companies in the fields of Autonomous Driving and Medical Devices and is currently working with Boston Scientific. He holds a PhD in Electrical and Computer Engineering from the University of Patras, Greece, as well as an MSc and MEng in related fields. Throughout his career, he has combined academic roles with industry positions focused on applied research and development in Computer Vision and Pattern Recognition, and has contributed to advancing methods in Computer Vision both through research published in peer-reviewed international journals and conferences and through cutting-edge research for product development, including projects at various stages from concept to commercialization.

Peter Corcoran (Fellow, IEEE) currently holds the Personal Chair of Electronic Engineering with the College of Science and Engineering, University of Galway. He was the Co-Founder of several start-up companies, notably FotoNation (currently the Imaging Division, Xperi Corporation). He has more than 600 cited technical publications and patents, more than 120 peer-reviewed journal articles, 160 international conference papers, and a co-inventor on more than 300 granted U.S. patents. He is an IEEE fellow recognized for his contributions to digital camera technologies, notably in-camera red-eye correction and facial detection. He is also a member of the IEEE Consumer Technology Society for more than 25 years and the Founding Editor of IEEE Consumer Electronics Magazine.

Appendix A. Random Feature Selection – Ablation Study

Table 9. Feature Random Selection Ablation Study – Accuracy

Layer	100	200	500	600	1000	1500
Run 1-Conv_1	0.525	0.522	0.850	0.856	0.853	0.847
Run 1-Conv_2	0.497	0.497	0.861	0.861	0.869	0.831
Run 1-Conv_3	0.506	0.533	0.797	0.797	0.792	0.817
Run 1-Bottleneck	0.500	0.500	0.500	0.500	0.500	0.494
Run 2-Conv_1	0.503	0.775	0.842	0.864	0.867	---
Run 2-Conv_2	0.519	0.519	0.850	0.811	0.819	---
Run 2-Conv_3	0.511	0.517	0.811	0.797	0.797	---
Run 2-Bottleneck	0.500	0.500	0.500	0.500	0.500	---
Run 3-Conv_1	0.514	0.511	0.861	0.875	0.844	---
Run 3-Conv_2	0.514	0.511	0.831	0.864	0.847	---
Run 3-Conv_3	0.514	0.519	0.803	0.789	0.803	---
Run 3-Bottleneck	0.500	0.500	0.500	0.500	0.500	---
Avg-Conv_1	0.514	0.603	**0.851**	**0.865**	**0.855**	---
Avg-Conv_2	0.510	0.509	**0.847**	**0.845**	**0.845**	---
Avg-Conv_3	0.510	0.523	0.804	0.794	0.797	---
Avg-Bottleneck	0.500	0.500	0.500	0.500	0.500	---

Table 10. Random Selection Ablation Study – Time to Test

Layer	100	200	500	600	1000
Conv_1	19.4 ms	34.6 ms	49.6 ms	52.3 ms	134.2 ms
Conv_2	19.1 ms	30.6 ms	**48.2 ms**	51.9 ms	131.9 ms
Conv_3	17.6 ms	30.2 ms	44.8 ms	50.1 ms	131.2 ms
Bottleneck	11.5 ms	14.3 ms	12.4 ms	12.2	12.0 ms

Appendix B. Optimisation of Backbone Autoencoder

Table 11. Autoencoder Architecture Optimisation – Step 1

Parameter Name	Fix parameter or Search Range
Encoder filters per layer and number of layers	[(32, 64, 96), (32, 64, 128), **(32, 64, 96, 128),** **(16, 32, 64, 128),** (16, 32, 96, 128, 160), (16, 32, 96, 128, 160, 192), (32, 64, 128, 256), (32, 64, 128, 256, 512)]
Learning Rate	0.00001 to 0.01
Number of Epochs	20 to 100
Optimiser Function	[**Adam**, SGD, RMSProp]
Loss function	[mse, mae, ssim]
Dropout rate	(0.0, 0.5) (uniform) [**0.11228**]

Table 12. Autoencoder Architecture Optimisation – Step 2

Parameter Name	Fix parameter or Search Range
Encoder filters	[(16, 32, 64, 128), (**32, 64, 128, 256**)] (categorical indices)
Batch size	[16, 32, 64, 128] (categorical)
Learning Rate	0.001 to 0.01 (uniform)
Number of Epochs	40 to 100 (uniform)
Optimiser Function	**Adam** (fixed)
Optimiser Parameters	β1: (0.90, 0.99) (uniform) β2: (0.9990, 0.9999) (uniform) epsilon: (10-8, 10-5) (uniform)
Loss function	[**mse**, mae, ssim] (categorical)

Appendix C. Thresholding ablation study

Table 13. Attention AE Anomaly Detection Thresholding Accuracy μ+2σ vs 95th Percentile

Model	ACC (μ+2σ)	ACC (95th Percentile)
MSE	0.742	**0.767**
SSIM	**0.875**	0.864
PSNR	0.739	**0.767**
MAE	0.817	**0.833**
MS-SSIM	**0.869**	0.858
4-SSIM	**0.864**	0.850
4-MS-SSIM	**0.903**	0.886
4-G-SSIM	**0.500**	0.483
4-MS-G-SSIM	0.553	**0.767**